ASSESSMENT OF VOLUMETRIC ENERGY DENSITY INFLUENCE ON MICROSTRUCTURE, DENSITY AND ROUGHNESS OF SELECTIVE LASER MELTING MANUFACTURED IN 625

Mihaela Raluca CONDRUZ[1*], Gheorghe MATACHE[1], Alexandru PARASCHIV[1], Teodor Adrian BADEA[1], Tiberius Florian FRIGIOESCU[1], Cornel TODEA[2]

Volumetric energy density (VED) influence on microstructural features, density and roughness of selective laser melting (SLM) manufactured IN 625 alloy was assessed based on computational and experimental analysis. VED values were defined and used to manufacture two batches of prismatic specimens applying two scanning strategies (90°, 67°). The computational automata finite element method was used to highlight the VED influence on microstructural texture and on the cooling rate. Experimentally was determined that the primary dendrite arm spacing, relative density and roughness are influenced by VED and the scanning strategy. It was concluded that VED can be effectively to manage some characteristics of SLM manufactured IN 625.

Keywords: VED, SLM, IN 625, density, microstructure

1. Introduction

Additive manufacturing (AM) technologies are considered among the main tools used to improve the European industrial competitiveness [1] and therefore during the last two decades many researchers in material science field focused their efforts on studying AMed metallic materials. Such advanced manufacturing technologies can be used in order to develop new complex designs and integrate them in many industrial fields such as aerospace and energy industries, but also in medicine [2, 3].

The main AM methods used to manufacture metallic parts are powder bed fusion (that includes the selective laser melting – SLM and electron beam melting processes – EBM) and directed energy deposition (that includes the laser engineered net shaping – LENS, electron beam freeform fabrication – EBF^3). As different metallic powder feedstocks are used, many process parameters of AM

[1] Scientific researchers, National Research and Development Institute for Gas Turbines COMOTI, Bucharest, Romania, raluca.condruz@comoti.ro, gheorghe.matache@comoti.ro, alexandru.paraschiv@comoti.ro, teodor.badea@comoti.ro, tiberius.frigioescu@comoti.ro

[2] Engineer, SC PLASMA TERM SA, 540390, Targu Mures, Romania, cornel.todea@plasmaterm.ro

machines are adjusted, to produce the metallic materials that are characterized by anisotropic characteristics and distinct performances [4]. So far, no optimum process parameters were defined to be used for each metallic material and each AM machine. In the case of powder bed fusion several researchers are studying the material characteristics based on a key factor, namely volumetric energy density (VED) [5-8] that integrates several process parameters.

Even if some authors sustain that this factor can be used to control the characteristics of AMed materials, others support the idea that VED equation should be optimized in order to include material properties and other process related characteristics [9-11]. Thereby, future studies should be conducted regarding the applicability of VED as a design parameter for AMed metals.

To develop new products many computational methods are applied during the designing phase. By computational modeling, the influence of many process variables on the product characteristics is studied aiming to reduce the overall manufacturing costs and material losses. As high costs are implied by these advanced manufacturing technologies, the use of computational methods is justified. A significant aspect that highly affects the properties of AMed metals is the microstructural development [12] which can be investigated by computational methods. Several models used for conventional manufactured metals were tailored for AM in order to predict their microstructural development [13-16].

The present study is focused on the assessment of the VED influence on the microstructural features, density and roughness of SLM manufactured IN 625. To highlight if VED can be employed as a designing parameter for Inconel alloy (IN 625), both computational and experimental methods were used.

2. Materials and methods

Prismatic specimens (10x10x20 mm^3) were manufactured using a DMG MORI Lasertec 30 SLM machine and IN 625 metal powder produced by LPW Technology Ltd, characterized by a median particle size of a cumulative volume distribution $d_{50,3}$ = 34 μm. Based on a simplified 3^3 factorial design of experiments (DOE), three levels of laser power, scanning speeds and hatch distances were used, while the layer thickness was kept constant (50 μm). The resulting VED values were calculated using Equation (1).

$$\text{VED} = \frac{P}{\nu \cdot h \cdot t} \ [\text{J} / \text{mm}^3] \tag{1}$$

Where: P is the laser power (W), ν is the scanning speed (mm/s), *h* is the hatch distance (mm) and *t* is layer thickness (mm).

Since the VED value calculated for the case #3 is too low, the experiment was replaced using the machine preset parameters (case #10). The resulting VED values used for specimen manufacturing process are presented in Table 1.

Table 1

Process parameters used for VED values definition

Case	Laser power, W	Scanning speed, m/s	Hatch distance, µm	VED, J/mm^3
1	170	0,6	90	63
2	170	0,8	110	39
~~3*~~	~~170~~	~~1,0~~	~~120~~	~~28~~
4	250	0,6	120	69
5	250	0,8	90	69
6	250	1,0	110	45
7	320	0,6	110	97
8	320	0,8	120	67
9	320	1,0	90	71
10**	242	0,73	110	60

* low VED value
** replaces the third case

Two specimen batches were manufactured applying two different scanning strategies, respectively a 90° and 67° scanning strategy, rotated by 90° between two successive layers. Each batch consisted in six groups of nine specimens placed in the same position (Figure 1).

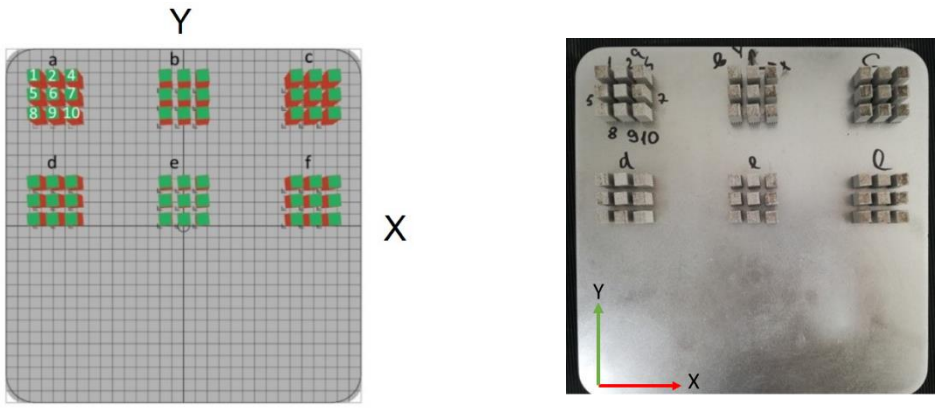

(a) (b)

Figure 1. Specimens placed on building plate: a) image from machine software; b) manufactured specimens on the building plate

Density and roughness measurements were realized on all specimens and the average values were reported as a function of VED. The material's density was determined on as-built specimens once the support material was removed by

grinding. The Archimedes method according to ISO 3369 standard was applied, using the Pioneer PX224 analytical balance with a density kit for solids. All measurements were realized using 99.3% purity ethanol as fluid, at room temperature.

Roughness (Ra) measurements were realized on specimens' sides (YZ plane) using the MarSurf PS 10 mobile roughness measuring instrument with an evaluation length of 12.5 mm according to DIN EN ISO 4288 standard.

Microstructural simulations were performed using the ANSYS Additive Suite, Additive Science module, R1/2020 edition. The simulations were realized for three VED values (39 J/mm³ - case #2, 69 J/mm³ - case #5 and 97 J/mm³ - case #7) using the same process parameters as in case of experimental procedure except for the laser beam diameter, which for the simulation was 80 µm (the software's lowest limit) and for experimental procedure was 70 µm. However, the IN 718 superalloy was used for simulations because it is the only Ni-based superalloy available in the ANSYS Additive Suite database validated for microstructural prediction. Both IN 625 and IN 718 are part of the same Ni-Cr class and the simulation results can be used as guidance in order to highlight microstructural aspects of additive manufactured microstructure.

Microstructural investigation by scanning electron microscopy (SEM) was realized using the SEM FEI Inspect F50. It was performed on the as-built material on the XY plane (specimen's top view) and in YZ plane (specimen's lateral view), and also on metalographically prepared specimens on YZ plane, after grinding, polishing and etching with aqua regia.

Primary dendrite arm spacing (PDAS) measurements were realized on backscattered electron SEM images taken at 15,000x magnification in different areas of specimens manufactured using the three above-mentioned VED values and both scanning strategies. The same type of measurements was done for cells spacing to emphasize the VED influence on the cellular morphology. For this purpose, Scandium software was used. The average primary dendrite arm spacing value was determined based on measurements realized on 8 different SEM images, while the spacing between cells was determined based on 5 measurements realized on 4 different SEM images. All dendrite arm and cell spacings were measured by intersection method using Equation (2). The results obtained were reported as a function of VED and the predicted cooling rate (CR).

$$PDAS = \frac{L}{d-1} \tag{2}$$

Where: L is the measuring length, d is dendrite/cell number identified on the L length.

3. Results and Discussions

3.1. Density and roughness measurements

The relative density of the produced material was calculated as the ratio between the measured density and the theoretical density of IN 625 (8.49 g/cm^3) calculated based on the actual chemical composition of the metal powder. The average relative density evolution for the two scanning strategies as a function of VED values is presented in Figure 1.

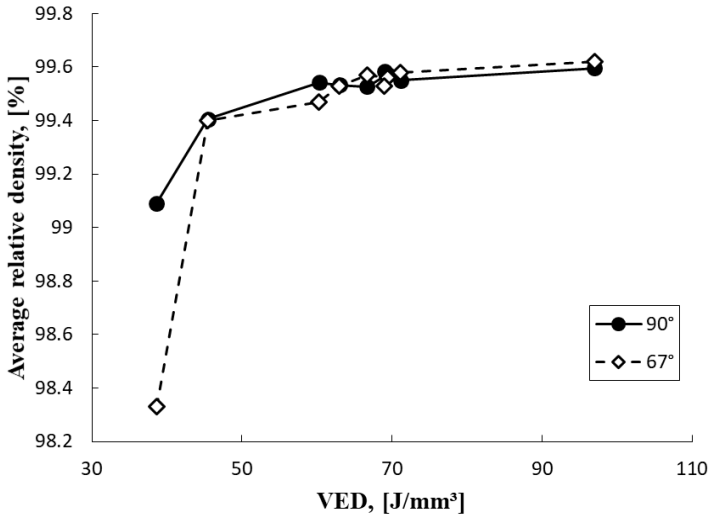

Fig. 1. Average relative density evolution as a function of VED for the two scanning strategies used (90° and 67°)

As the VED increases the material becomes denser. The highest densification level was registered for samples manufactured using the highest VED (97 J/mm^3), 99.60% when the 90° scanning strategy was applied and 99.63% when the 67° scanning strategy was applied.

It was observed that at low VED values the influence of the scanning strategy is more noteworthy compared with the influence noticed at higher VED values. For a VED of 39 J/mm^3 the 90° scanning strategy ensured a 99.09% relative density while the 67° scanning strategy ensured only 98.33% relative density. It can be concluded that the 67° scanning strategy leads to both the lowest and the highest material's densification degree as a function of VED.

The density variations using different VED values are caused by defects occurrence and mainly by the lack of fusion (LOF) defects observed in the XY plane. Based on SEM analysis it was determined that the LOF level reduces as the VED increases. Representative SEM images with the LOF evolution as a function

of VED for specimens manufactured using a 90° scanning strategy are presented in Figure 2.

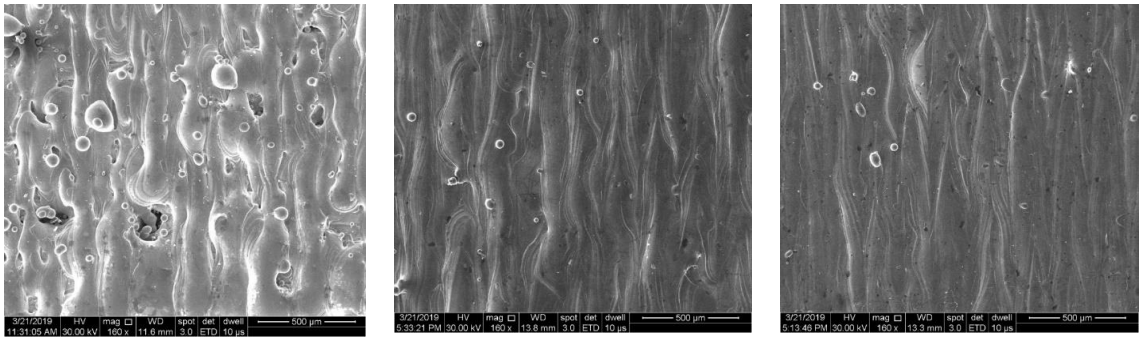

(a) (b) (c)

Fig. 2. SEM images (XY plane) that show the LOF evolution as a function of VED: a) VED – 39 J/mm^3; b) VED – 69 J/mm^3; c) VED – 97 J/mm^3

The results obtained in case of SLM manufactured IN 625 are in a good agreement with the results obtained by Darvish et.al. [17] for SLM manufactured CoCrMo. They observed that at low laser powers (180 W), the melt track couldn't ensure overlapping and thereby the LOF defects form. Moreover, increasing the laser power up to 300W the LOF level is reduced, but another defect emerges, such as large spatter that form due to melt pool instability.

Spatter formation was observed as well in the current study, and it is also influenced by VED. An increase in VED causes an increase in spatter quantity, as it can be observed in SEM images from Figure 3 taken for specimens manufactured using a 67° scanning strategy.

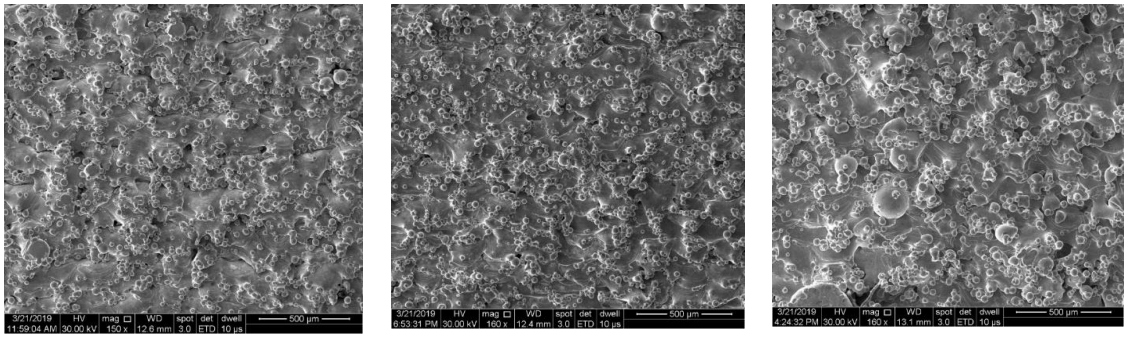

(a) (b) (c)

Fig. 3. SEM images (YZ plane) that show the spatter evolution as a function of VED: a) VED – 39 J/mm^3; b) VED – 69 J/mm^3; c) VED – 97 J/mm^3

The increase quantity of spatter affects the material's surface finish, respectively the surface roughness. The average roughness evolution as a function of VED is presented in Figure 4. It was determined that the increase in VED causes an increase of the average Ra. Besides VED, it was concluded that the scanning strategy has a slight influence on the surface roughness. The 67° scanning strategy generates in some respect higher Ra values compared with the 90° scanning strategy. The influence of process parameters on additive manufactured metals' roughness was also determined by other authors [18-20] and shows a similar behavior.

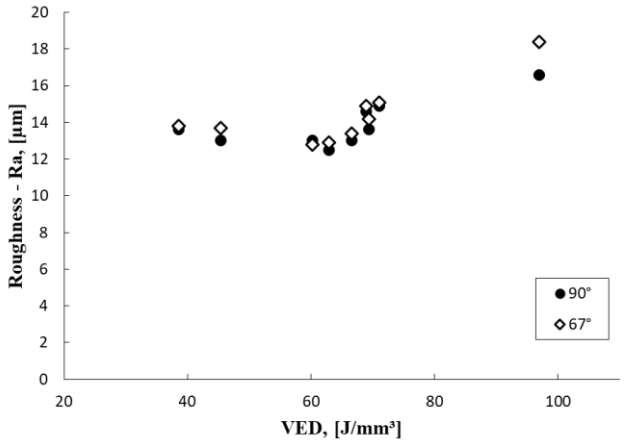

Fig. 4. The average roughness evolution as a function of VED

3.2. Microstructural simulations

As in case of density and roughness analyses, the simulations highlighted the influence of VED on the as-built microstructure, as it can be observed in Figures 5 and 6, where 3D microstructure reconstructions based on simulation results of specimens manufactured using different VED values and both scanning strategies are presented.

As it can be observed in the images from Figures 5 and 6, the as-built microstructure is characterized by a high texture. The increase of VED ensures the growth of long columnar grains along the Z axis (as it can be observed on planes XZ and YZ) that develop over multiple layers and also an increase of the equiaxed grains developed on the XY plane, regardless of the scanning strategy used.

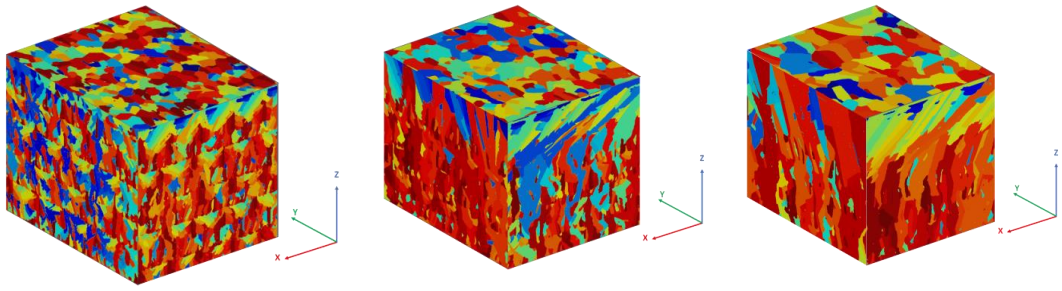

(a) (b) (c)

Fig. 5. Simulation results for microstructural evolution for the material manufactured using a 90°scanning strategy, as a function of VED: a) 39 J/mm^3; b) 69 J/mm^3; c) 97 J/mm^3

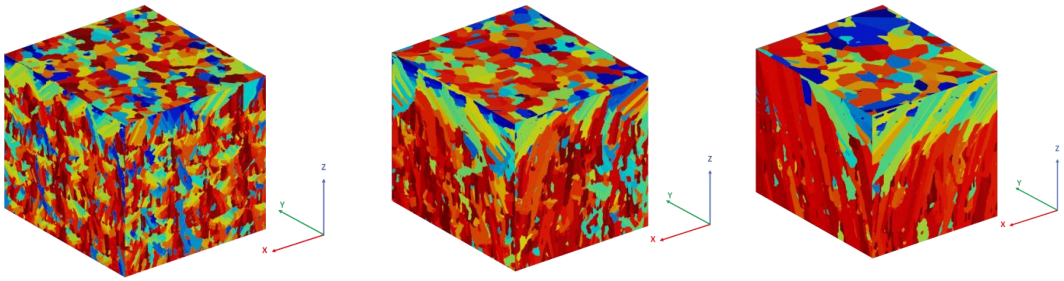

(a) (b) (c)

Fig. 6. Simulation results for microstructural evolution for the material manufactured using a 67° scanning strategy, as a function of VED: a) 39 J/mm^3; b) 69 J/mm^3; c) 97 J/mm^3

Using the ANSYS predictions, the evolution of the grain size determined by the circle equivalence method was realized. Figure 7 presents the grain size evolution as a function of VED for the two scanning strategies.

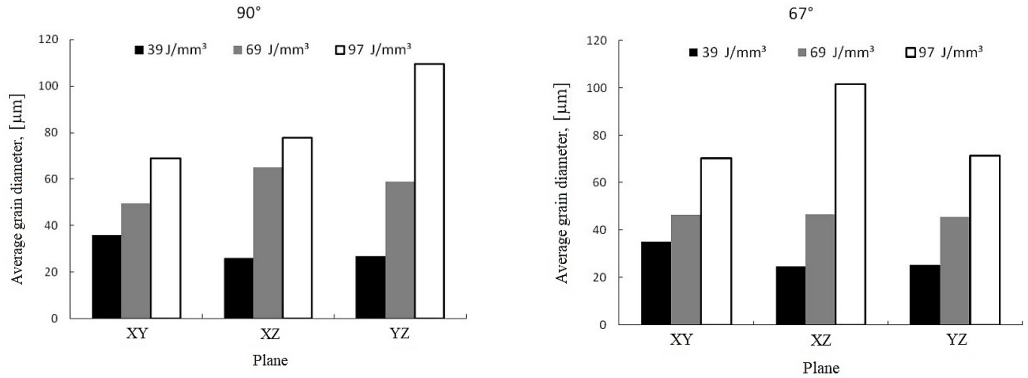

(a) (b)

Fig. 7. Grain size evolution as a function of VED and scanning strategy at 90° (a), respective 67° (b)

As it was noticed from Figures 5 to 7 the finest microstructural features were registered in case of low VED values, as the cooling rates are very high. The simulation software predicts for the batch manufactured using the 90° scanning strategy, a CR of 6.59 x 10^5 K/s and a thermal gradient (G) of 5.47 x 10^6 K/m for specimens manufactured using a 39 J/mm^3 VED reaching a CR of 1.93 x 10^5 K/s and a G of 2.99 x 10^6 K/m for specimens manufactured using a 97 J/mm^3 VED. For the batch manufactured using 67° scanning strategy and 39 J/mm^3 VED a CR of 6.52 x 10^5 K/s and a G of 5.45 x 10^6 K/m, reaching a CR of 1.98 x 10^5 K/s and a G of 3.11 x 10^6 K/m for specimens manufactured using the 97 J/mm^3 VED. The simulations shown that the CR is inversely proportional to VED, regardless of the scanning strategy used.

The software also predicts the melt pool dimensions before it solidifies in terms of depth, length and width. An increase in VED value causes also an increase in melt pool size, as it can be observed in Figure 8.

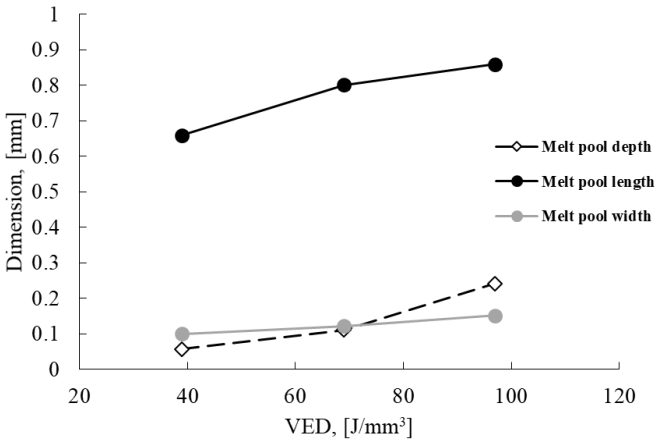

Fig. 8. Melt pool size as a function of VED

3.3. Experimental microstructural investigations

Microstructural investigations were realized in order to determine the VED influence on the spacing between columnar dendrites and cells. The evolution of PDAS as a function of VED and the CR is presented in Figure 9. To highlight the differences, representative SEM images are presented in Figures 10 and 11.

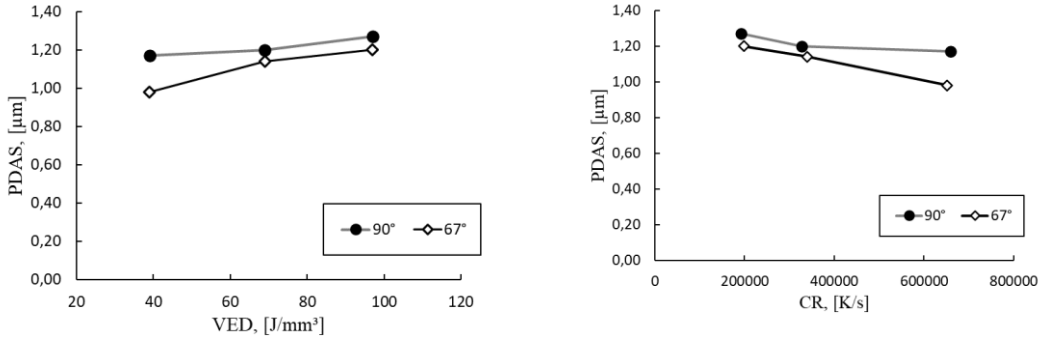

(a) (b)

Fig. 9. Evolution of primary dendrite arm spacing as a function of VED (a) and CR (b)

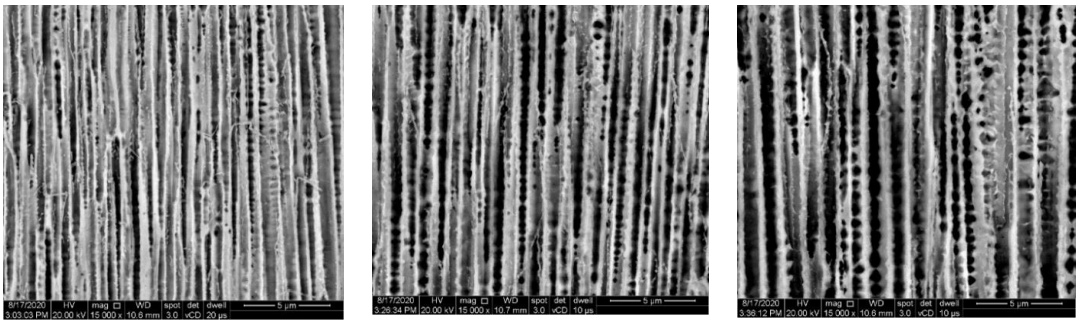

(a) (b) (c)

Fig. 10. Representative SEM images (YZ plane) with the columnar dendrites in case of specimens manufactured using the 90° scanning strategy, as a function of VED: a) VED = 39 J/mm^3; b) VED = 69 J/mm^3; c) VED = 97 J/mm^3

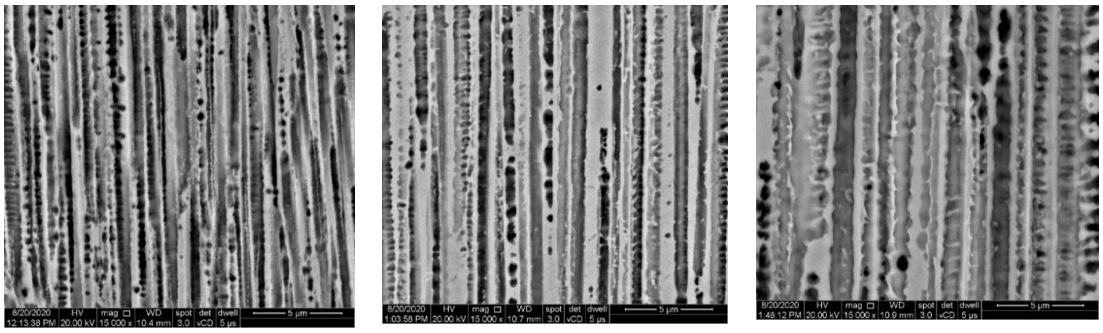

(a) (b) (c)

Fig. 11. Representative SEM images (YZ plane) with the columnar dendrites in case of specimens manufactured using the 67° scanning strategy, as a function of VED: a) VED = 39 J/mm^3; b) VED = 69 J/mm^3; c) VED = 97 J/mm^3

The primary dendrite arm spacing is directly proportional with the VED values, but indirectly proportional with the CR values. For a better understanding

of the results, the registered PDAS were compared with the values reported in a previous work by Matache et.al. [21] for much lower cooling rates for a single-crystal Ni-based superalloy manufactured using the Bridgman method as it can be seen in Figure 12.

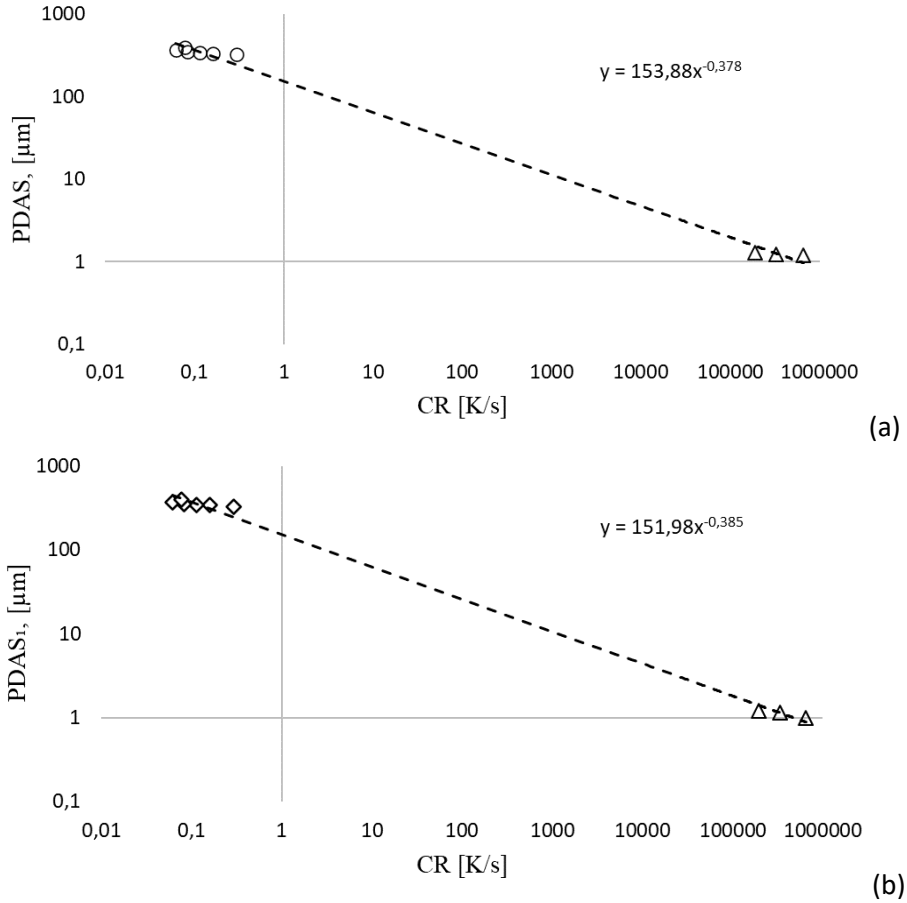

Fig. 12. PDAS values reported for columnar dendrites as a function of the cooling rate: a) results obtained in case of the additive manufactured IN 625 using the 90° scanning strategy; b) results obtained in case of the additive manufactured IN 625 using the 67° scanning strategy (where the values determined for the AMed material are marked with triangles)

It was observed that for the whole data range from very low (Bridgman method) to extremely high (SLM) cooling rates, PDAS follows the relation PDAS $=153{,}88\cdot(R)^{0{,}378}$ for the material manufactured using the 90° scanning strategy, respective PDAS$=151{,}98\cdot(R)^{0{,}385}$ for the material manufactured using the 67° scanning strategy. These relations are in good agreement with the theoretical relation $PDAS = ct.(R)^{0{,}3\pm0{,}03}$ [22], and also with the relation calculated by

Matache et.al. [21] PDAS=151,98·$(R)^{0,34}$ in the case of the single-crystal Ni-based superalloy.

The differences are caused by the higher cooling rates registered for the additive manufactured material. Moreover, the experimental data follows the same trend as the values reported by Zhang et.al. [23] for different cast Ni-based superalloys.

The same evolution was observed also for the cells size, as it can be observed in Figures 13-15. The analysis of spacing between columnar dendrite and cells revealed that the VED has a higher influence on the distance between cells as compared with the distance between the columnar dendrites.

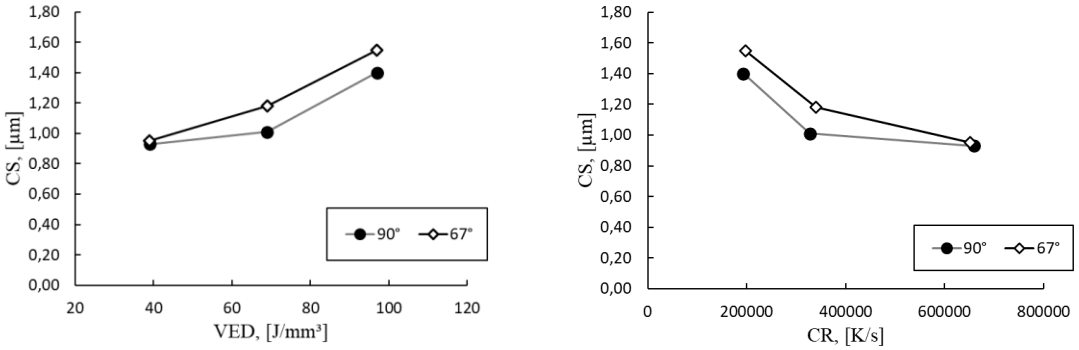

Fig. 13. Evolution of cells' spacing as a function of VED (a) and CR (b)

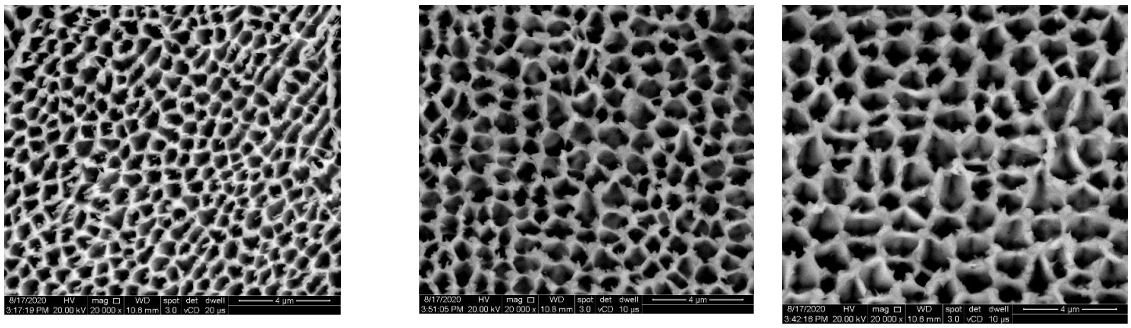

(a) (b) (c)

Fig. 14. Representative SEM images (YZ plane) with the cells in case of specimens manufactured using the 90° scanning strategy, as a function of VED: a) VED = 39 J/mm^3; b) VED = 69 J/mm^3; c) VED = 97 J/mm^3

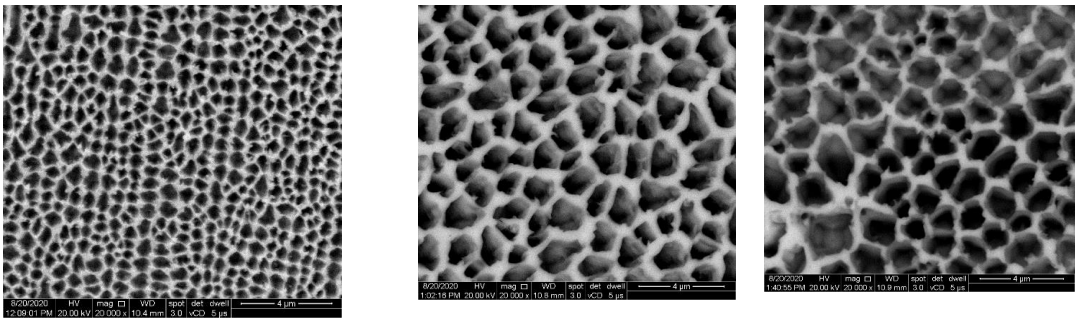

(a) (b) (c)

Fig. 15. Representative SEM images (YZ plane) with the cells in case of specimens manufactured using the 67° scanning strategy, as a function of VED: a) VED = 39 J/mm^3; b) VED = 69 J/mm^3; c) VED = 97 J/mm^3

4. Conclusions

The influence of VED on microstructural features, relative density and roughness of SLM manufactured IN 625 was assessed based on computational and experimental results. It was highlighted that VED has a significant influence on all investigated aspects. As the VED increases, the materials become denser by reducing the level of LOF defects.

Regardless of the scanning strategy used, the highest VED value (97 J/mm^3) ensures a densification level of the alloy higher than 99.5%. The scanning strategy has a low influence on the material's densification level at high VED values, but a significant influence in case of using low VED values. High VED values generate higher surface roughness as sputter forms due to melt pool instability.

The microstructural simulations revealed the VED influence on the material's microstructural development in terms of microstructural texture, grain size, cooling rate and melt pool size. The grain size increases along with VED increasing due to a change in melt pool dimensions, especially melt pool's depth. As the laser penetration depth increases, partial remelting of previous deposited layers occurs and the material's cooling rate decreases.

Experimentally it was determined that an increase in VED allows the dendrites/cells to grow, increasing the space between them, regardless of the scanning strategy used.

Adding up the spacing dimensions, as a function of cooling rate, for both additive manufactured material and for a single-crystal Ni-based superalloys revealed a good agreement between the results registered with respect to the dendrites arm spacing as a function of cooling rate.

The general conclusion of the study is that VED parameter can be used as a designing parameter in relationship with the densification, roughness and microstructural development for IN 625 manufactured by SLM. Future studies will be conducted to determine if VED can be also used for designing the mechanical properties of SLM manufactured IN 625.

Acknowledgement

This work was supported by POC-A1-A1.2.3-G-2015, ID/SMIS code: P_40_422/105884, "TRANSCUMAT" Project, Grant no. 114/09.09.2016 (Subsidiary Contract no. 6/D.1.4/114/18.06.2018), Project funded by the Romanian Minister of Research and Innovation.

R E F E R E N C E S

[1]. *D.S. Gonzalez, A. Gonzalez Alvarez,* Additive Manufacturing Feasibility Study & Technology Demonstration, European Defense Agency AM State of the Art & Strategic Report, 2018

[2]. *L. Yang, K. Hsu, B. Baughman, D. Godfrey, F. Medina, M. Menon, S. Wiener*, Additive Manufacturing of Metals: The Technology, Materials, Design and Production, Springer Series in Advanced Manufacturing (Ed. D.T. Pham), 2017

[3]. *J.O. Milewski*, Additive Manufacturing of Metals. From Fundamental Technology to Rocket Nozzles, Medical Implants, and Custom Jewelry, Springer Series in Materials Science (Ed. R.Hull, C. Jagadish, Y. Kawazoe, R.M. Osgood, J. Parisi, T.Y. Seong, S.Uchida, Z.M. Wang), 2017

[4]. *T.DebRoy, H.L.Wei, J.S.Zuback, T.Mukherjee, J.W.Elmer, J.O.Milewski, A.M.Beese, A.Wilson-Heid, A.DedW.Zhang*. Additive manufacturing of metallic components – Process, structure and properties. Progress in Materials Science, **vol.** 92, Mar. 2018, pp. 112-224

[5]. *C. Duan, M. Zhao, X. Luo,* Thermal Behavior and Densification Mechanism during Selective Laser Melting Additive Manufacturing of Metal Powder, Steel Research International, **vol. 91**, Issue 8, Aug. 2020, 2000073.

[6]. *T. Peng, C. Chen*, Influence of energy density on energy demand and porosity of 316L stainless steel fabricated by selective laser melting, International Journal of Precision Engineering and Manufacturing-Green Technology, **vol. 5**, 2018, pp. 55–62

[7]. *H. Gu, H. Gong, D. Pal, K. Rafi, T. Starr*, Brent Stucker Influences of Energy Density on Porosity and Microstructure of Selective Laser Melted 17- 4PH Stainless Steel, 24th Annual International Solid Freeform Fabrication Symposium Conference, 12-14 Aug. 2013, Austin, Texas, USA

[8]. *V. Gunenthiram, P. Peyre, M. Schneider, M. Dal, F. Coste, I.Koutiri, R. Fabbro*, Experimental analysis of spatter generation and melt-pool behavior during the powder bed laser beam melting process, Journal of Materials Processing Technology, **vol. 251**, Jan. 2018, pp. 376-386.

[9]. *K. G. Prashanth,S. Scudino, T. Maity, J. Das, J. Eckert*, Is the energy density a reliable parameter for materials synthesis by selective laser melting?, Journal Materials Research Letters, **vol. 5**, Issue 6, 2017, pp. 386-390

[10]. *U. Scipioni Bertoli, A. J. Wolfer, M. J.Matthews, J.-P. R. Delplanque, J. M. Schoenung*, On the limitations of Volumetric Energy Density as a design parameter for Selective Laser Melting, Materials & Design, **vol. 113**, Jan. 2017, pp. 331-340.

[11]. *P. Ferro, R. Meneghello, G. Savio, F. Berto*, A modified volumetric energy density–based approach for porosity assessment in additive manufacturing process design, The International Journal of Advanced Manufacturing Technology, **vol. 110**, Aug. 2020, pp. 1911–1921

[12]. *Y. Kok, X.P. Tan, P. Wang, M.L.S. Nai, N.H. Loh, E. Liua, S.B. Tora*, Anisotropy and heterogeneity of microstructure and mechanical properties in metal additive manufacturing: A critical review, Materials & Design, **vol. 139**, Feb. 2018, pp. 565-586

[13]. *T. M. Rodgers, J. D. Madison, V.Tikare*, Simulation of metal additive manufacturing microstructures using kinetic Monte Carlo, Computational Materials Science, **vol. 135**, Jul. 2017, pp. 78-89.

[14]. *J. Zhang, L. Yan, W. Li, F. Liou*, A Two-Dimensional Simulation of Grain Structure Growth within Substrate and Fusion Zone during Direct Metal Deposition, Book Additive Manufacturing of High-performance Metals and Alloys - Modeling and Optimization (I. Shishkovskey Ed.), Jan. 2018, pp. 11-32

[15]. *J. Li, X. Zhou, M. Brochu, N. Provatas, Y. F. Zha*o, Solidification microstructure simulation of Ti-6Al-4V in metal additive manufacturing: A review, Additive Manufacturing, **vol. 31**, Jan. 2020, 100989

[16]. *A. Zinoviev, O. Zinovieva, V. Ploshikhin, V. Romanova, R. Balokhonov*, Evolution of grain structure during laser additive manufacturing. Simulation by a cellular automata method, Materials & Design Volume, **vol. 106**, Sept. 2016, pp. 321-329

[17]. *K. Darvish, Z.W. Chen, T. Pasang*, Reducing lack of fusion during selective laser melting of CoCrMo alloy: Effect of laser power on geometrical features of tracks, Materials & Design, **vol. 112**, Dec. 2016, pp. 357-366

[18]. *A. Charles, A. Elkaseer, L. Thijs, V. Hagenmeyer, S. Scholz*, Effect of Process Parameters on the Generated Surface Roughness of Down-Facing Surfaces in Selective Laser Melting, Applied Sciences, 2019, **vol. 9** (6), Mar. 2019, 1256

[19]. *K. Mumtaz, N. Hopkinson,* Top surface and side roughness of Inconel 625 Parts processed using selective laser melting, Rapid Prototyping Journal, **vol. 15**, no. 2, 2009, pp. 96–103

[20]. *A. Safdar, H.Z. He, L.-Y. Wei, A. Snis, L. E. Chavez de Paz*, Effect of process parameters settings and thickness on surface roughness of EBM produced Ti-6Al-4V, Rapid Prototyping Journal, **vol. 18**, no. 5, 2012, pp. 401-408

[21]. *G. Matache, D. M. Stefanescu, C. Puscasu, E. Alexandrescu, A. Bührig-Polaczek*, Investigation of solidification microstructure of single crystal CMSX-4 superalloy – experimental measurements and modelling predictions, International Journal of Cast Metals Research, vol. 28, issue 6, 2015, pp. 323-336

[22]. *D.M. Stefanescu*, Cresterea celulara si dendritica, in Stiinta si Ingineria solidificarii pieselor turnate, Ed. Agir, 2007, pp. 207-258

[23]. *Y. Zhang, B. Huang, J. Li*, Microstructural Evolution with a Wide Range of Slidification Cooling Rates in A Ni-Based Superalloy, Metallurgical and Materials Transactions A, **vol. 44**, 2013, pp. 1641-1644